NANO EXPRESS

Multiscale Simulation of Indentation, Retraction and Fracture Processes of Nanocontact

Jifa Mei · Junwan Li · Yushan Ni · Huatao Wang

Abstract The process of nanocontact including indentation and retraction between a large Ni tip and a Cu substrate is investigated using quasicontinuum (QC) method. The multiscale model reveals that significant plastic deformation occurs during the process of nanocontact between Ni tip and Cu substrate. Plastic deformation is observed in an area as large as 20 nm wide and 10 nm thick beneath Ni tip during the indentation and retraction. Also, plastic deformation at a deep position in the Cu substrate does not disappear after the neck failure. The analysis of generalized planar fault energy curve shows that there is a strong tendency for deformation twinning in Cu substrate. However, deformation twinning will be retarded during indentation due to the high stress intensity caused by stepped surface of Ni tip. The abrupt drop of load curve during tip retraction is attributed to the two different fracture mechanisms. One is atomic rearrangement near the interface of Ni tip and Cu substrate at the initial stage of neck fracture, the other is shear behavior of adjacent {111} planes at the necking point. A comparison of the critical load and critical contact radius for neck fracture is also made between theoretical values and our numerical results.

Keywords Multiscale simulation · Quasicontinuum method · Nanocontact · Neck fracture

J. Mei · J. Li · Y. Ni (✉) · H. Wang
Department of Mechanics and Engineering Science,
Fudan University, 200433 Shanghai, China
e-mail: niyushan@fudan.edu.cn

Introduction

The intricate mechanical and thermal behavior of nano-sized contact not only is of fundamental importance involved in friction and wear process [1–3], but also plays a vital role in microelectromechanical/nanoelectromechanical systems (MEMS/NEMS) [4–6]. The understanding of the fundamental mechanisms of nanocontact at atomic scales has become one subject of intensive research. With the help of experimental techniques, such as atomic force microscopy (AFM), the scanning tunneling microscope (STM), confocal Raman microscopy (CRM), and the mechanically controllable break junction (MCBJ), lots of experimental studies have been carried out to investigate metallic contact and the process of indentation and retraction of nanocontact [7–11]. But it is still difficult to examine the real-time evolution of atomic configuration near contact area experimentally.

Molecular dynamics (MD) simulation is now extensively used to investigate nanocontacts for its potential to reveal detailed deformation mechanism at the atomic scale. For instance, the earliest MD simulations of nanocontact are carried out by Land et al. [12, 13] using a Ni tip with a radius of 3 nm; Song and Srolovitz [14, 15] have investigated the influence of the work of adhesion on material transfer in asperity contacts; Jiang et al. [16] studied the effects of strain rates on the plastic flow during nanoindentation by using molecular dynamics. Hagelaar [17] examined different types of deformation mechanisms when a tungsten tip and a tungsten substrate come into contact under different combinations of crystal direction. Although MD can provide insights into the formation, deformation, and fracture of nanocontacts, there are many disadvantages for MD simulations. One is that its limited timescale leads usually to unrealistic high pulling rates, and relatively small sizes of

MD may cause unrealistic boundary conditions which artificially change the dislocation dynamics. Furthermore, most of MD simulations are carried out with tip radiuses smaller than 5 nm while the radius of a typical tip used in tip–substrate interaction experiment by STM is around or even larger than 10 nm [7, 18, 19]. Recently, several multiscale methods [20–23] are proposed to simulate models with dimensions of the order of microns and thus minimize the possibility of the contamination of the results by the boundary conditions arising from the small model size.

Based on earlier discussions, we employ an efficient and effective multiscale method—quasicontinnum (QC) method initially developed by Tadmor et al. [24]— to investigate nanocontact process with large dimension of tip and substrate, which can effectively avoid the artificial boundary conditions encountered in MD. In present study, combined with the generalized planar fault energy (GPF) curve, we discuss the deformation twinning that is formed in the whole contact process. In addition, we find two different types of neck fracture mechanisms corresponding to the load-jump in the load–depth curve. Finally, a comparison of the critical load and critical contact radius for neck fracture is also made between adhesive contact model and our numerical results.

Simulation Method

The QC method is an effective multiscale approach that couples continuum and atomic simulation. It is established that discrete atomic description are only necessary at highly deformed region and in the vicinity of defects or interfaces. Representative atoms in QC method are divided into local atoms and non-local atoms. The local atoms capture the deformation behavior of atoms that undergo slowly varying deformation based on Cauchy–born rule. The non-local atoms are treated by discrete atomistic lattice statics in the areas where severe plastic deformations occur. By using an adaptive refinement strategy, the QC method automatically reduces the degrees of freedoms and computational demand without losing atomistic detail in regions where it is required. More details of QC method can be found in [25].

A schematic illustration of nanocontact between Ni tip and Cu substrate is shown in Fig. 1a. The radius of Ni tip in our model is 10 nm, much larger than most of tips used MD simulations as far as we know. A nickel tip is chosen because it is harder than Cu and tip deformation is not desired in experiments. The crystal directions of Ni tip along x and y axis are chosen to be $[\bar{1}10]$ and $[111]$, respectively. Along this lattice orientation, the Ni tip has higher stiffness. In this study, the geometry of Ni tip is modeled as a wedge with a tip radius of 10 nm, which is

similar to that used in experiment, as illustrated in Fig. 1a. The single crystal Cu substrate in this simulation is 200 nm wide, 100 nm thick, and infinite in the out-of-plane direction with periodic boundary conditions. The size of Cu substrate is one order magnitude larger than the typical models used in MD. The crystal directions of Cu substrate along x- and y-axis are chosen to be [110] and [001], respectively, to facilitate the emissions of Shockley partials and deformation twinning [26].

The selection of representative atoms near the interface is shown in Fig. 1b. In order to avoid initial interaction between the Ni tip and the upper surface of Cu substrate, the initial distance between them is 0.65 nm, which is larger than the cutoff radius (0.55 nm).During the simulation, the bottom of the substrate is kept fixed, and the left and right boundaries of the substrate are set free. The Ni tip is gradually indented or retracted from the Cu substrate by displacement-imposed boundary conditions with an
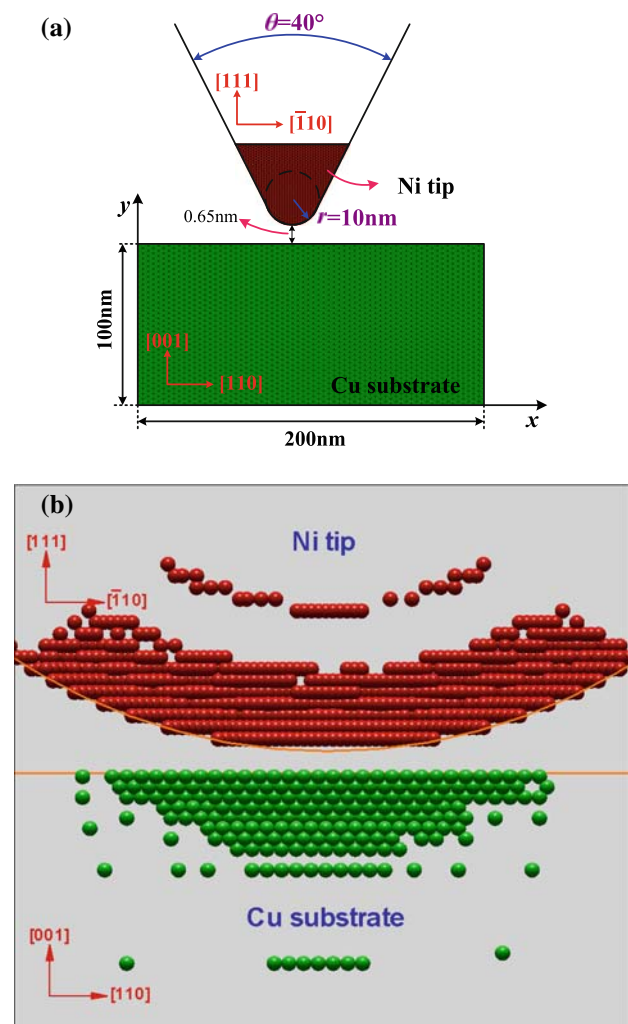

Fig. 1 Schematic representation of **a** naocontact model and **b** representative atoms near the interface

increment of 0.02 nm per step. The maximum of indentation depth is approximately 2 nm and subsequent the Ni tip retracts from the substrate completely. The interatomic interactions between the same types of atoms are described by the embedded-atom-method (EAM) potential developed by Daw and Baskes, [27] while different types of atoms (namely, Cu atoms and Ni atoms) described through the geometric mean of the pair interaction potential.

Results

The load as a function of indentation depth during the whole process of indentation and subsequent retraction is plotted in Fig. 2. The arrows illustrate the direction of motion of Ni tip. The load is the sum of the force acting on the top surface of Ni tip divided by the repeating distance along the out-of-plane direction. Positive load in Fig. 2 indicates the repulsive interaction between Ni tip and Cu substrate, while negative force refers to adhesive interaction. The initial contact between Ni tip and Cu substrate corresponds to zero indentation depth. A number of inflection points of interest are denoted by alphabetic characters. The whole process can be divided into two parts: indentation process (correspond to O–J stage of the load–depth curve in Fig. 2) and retraction process (correspond to J–V stage in Fig. 2). The von Mises strain [28] is used as a simple but sufficient tool to trace slipped atoms in our simulation though more elaborate ways of identifying defects are available.

Indentation Process

The initial distance between the atoms of the Ni tip and the surface atoms of the substrate is chosen to be larger than the cutoff radius (0.55 nm) of the intermolecular potential
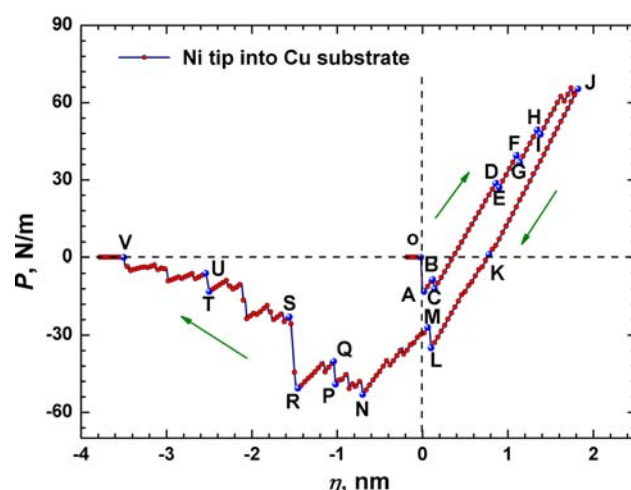

Fig. 2 Load–depth response curve for nanocontact

to avoid initial interaction. Ni tip jumps to contact with Cu substrate abruptly at a distance of 0.45 nm (corresponding to O–A stage in Fig. 2). Though jump-to-contact have also been observed by experiments [7, 12, 29] and MD simulation [17], our research further reveals that the strong localized attractive force (about 2.8 GPa) between large Ni tip and Cu substrate during jump-to-contact can lead to plastic deformation of Cu substrate. As shown in Fig. 3a, a hole in Cu substrate near the interface denoted by letter A is observed in our simulation. After the abrupt jump-to-contact, attractive force between the tip and the substrate decreases linearly until next load drop (namely, B–C stage) caused by annihilation of the hole occurs.

During C–D stage, a lack of special features and deflection points indicates that Cu substrate undergoes a long period of elastic deformation. After that, the increased load leads to the simultaneous emission of a $a/6[\bar{1}\bar{1}\bar{2}]$ (a is the lattice constant of Cu) Shockley partial along $(\bar{1}\bar{1}1)$ plane and a $a/6[\bar{1}\bar{1}\bar{2}]$ Shockley partial along (111) plane from the surface of Cu substrate (corresponding to the B–C stage shown in Fig. 2). The two Shockley partials interact beneath the tip, and a new dislocation is formed as shown in Fig. 3b. The interaction of Shockley partial is

$$\frac{1}{6}a[\bar{1}\bar{1}2] + \frac{1}{6}a[\bar{1}\bar{1}\bar{2}] = \frac{1}{3}a[\bar{1}\bar{1}0] \quad (1)$$

The new dislocation is also termed as nominal lock [30] since the Burger's vector of the dislocation is not along the slip direction and is constrained by the periodic boundary along out-of-plane direction. It is worth noting that Shockley partials emit from the surface of the substrate near the steps of Ni tip. This is quite different from the results that dislocations nucleate in the substrate beneath ideal rigid indenters [31, 32] which is represented by a sphere repulsive potential. Our result indicates that it is highly possible that Shockley partials emitted from the surface into Cu substrate first due to the irregularity of tip or surface roughness.

After elastic stage of E–F in Fig. 2, two Shockley partials emit along the $(\bar{1}\bar{1}1)$ and (111) plane from the surface again, and another lock is created when the two Shockley partials meet with each other. With the increase in indentation depth, the slip along on $(\bar{1}\bar{1}1)$ plane passes the lock and extends away from surface of substrate as seen in Fig. 3c. At the same time, a two-layer twinning fault in Cu is observed on the right-hand side of Cu substrate beneath Ni tip. Deformation twinning will be investigated by the GPF in later discussion.

Figure 3d illustrates atomic configuration at the maximum indentation depth. Both three-layer twinning faults and stacking faults are observed in the Cu substrate. It is surprising that the longest stacking fault extends into Cu substrate as deep as 14 nm, even larger than the dimensions

Fig. 3 Atomic configurations of Cu substrate during indentation process at different depth: **a** $\eta = 0.0$ nm, **b** $\eta = 0.9$ nm, **c** $\eta = 1.38$ nm and **d** $\eta = 1.82$ nm
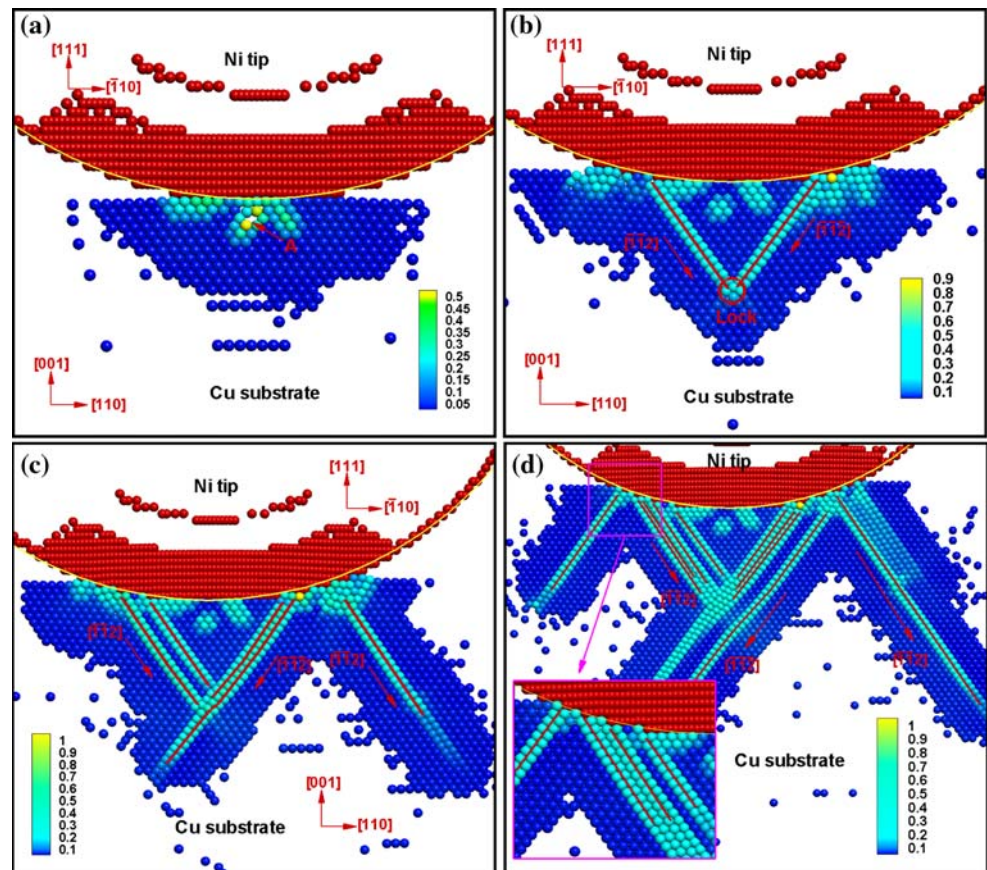
of some MD models. Besides, the stacking faults are also observed on the two sides of Ni tip. The plastic deformation occurs in an area as large as 20 nm wide and 10 nm thick at the end of the indentation. The large area of plastic deformation in our multiscale simulation indicates that MD simulations might not fully capture details of deformation during nanocontact with a relatively large tip.

Retraction Process

Retraction process can also be clearly classified into two parts based on the profile of load–depth curve in Fig. 2. During the first part of retraction (namely, J–L stages in Fig. 2), the load decreases linearly with the decrease of indentation depth, which is very similar to the unloading process of macroscopic compression test. For the second part (as M–V stages in Fig. 2), a neck is formed and then gradually break. This process is accompanied by sawtooth-shaped load-jump. Considering their distinguish characteristics, the two parts of retraction are discussed, respectively.

The Linear Part of Retraction

During the first part of retraction, the linear decrease of load with the reduction of indentation depth is observed in

our simulation, which is in agreement with the results of many experiments [8, 33, 34]. The linear decrease of load can be confirmed by careful examination of atomic configuration beneath Ni tip. Figure 4a shows the atomic configuration when completely unloaded (point K in Fig. 2). Comparing the atomic configuration at maximum indentation depth (Fig. 3d) with the unloaded one, we can find that almost none of stacking faults and twinning faults disappear during this unloading process. Further retraction also increases adhesive force almost linearly at K–L stages in Fig. 2. The jump of adhesive force at L–M stages is caused by the simultaneous backward slip of atoms on $(\bar{1}\bar{1}1)$ and (111) planes. Corresponding to the point M in Fig. 2, the atomic configuration is shown in Fig. 4b. It can be seen that only few stacking faults and twinning faults exist beneath Ni tip.

The Part of Neck Formation and Destruction

When Ni tip is gradually pulled out of Cu substrate, adhesive force between Ni tip and Cu substrate continues to increase first. The largest adhesive force (approximately 6.63 GPa) is arrived at point N in Fig. 2. This process of adhesive load increase during this part is accompanied by the formation of Cu neck. Compared with pressure-induced

Fig. 4 Atomic configurations of Cu substrate during the first part of retraction process at different depth: **a** $\eta = 0.76$ nm, **b** $\eta = 0.1$ nm
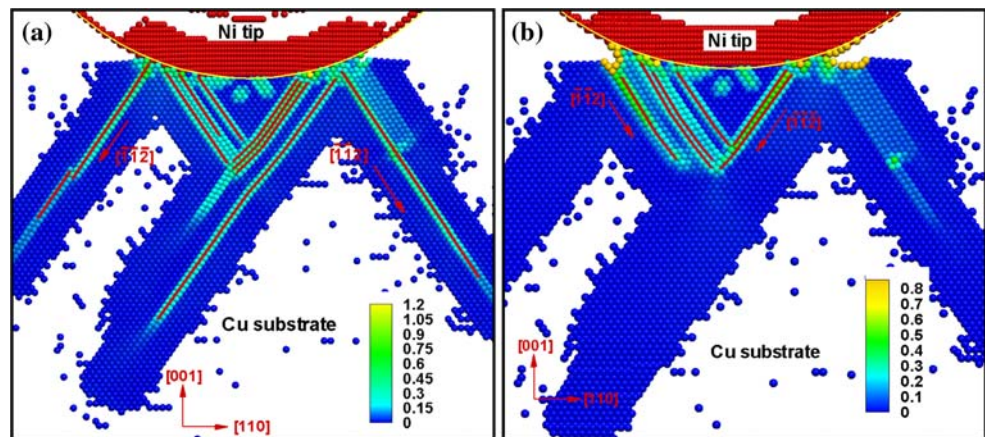
stacking faults and twinning faults during indentation, stacking faults and twinning faults are produced as a result of pulling force. The stacking faults and twinning faults are crucial for the formation and elongation of neck. This is illustrated in Fig. 5a, as atoms on $(\bar{1}\bar{1}1)$ and (111) planes begin to slip, Cu atoms encircled by the slip planes move upward. The more stacking faults or twinning faults beneath Ni tip, the longer the neck will be.

In accordance with sawtooth-shaped loads observed in experiments [33, 35], the irregular jumps of load–depth curve during unload process are shown in Fig. 2, as Ni tip is pulled out of Cu substrate. Our displacement-controlled simulation reveals clearly the underlying mechanism of irregular load-jump. We find that two main fracture mechanisms are responsible for the sawtooth-shaped load: the atomic rearrangement caused by stepped surface at the initial stage of neck break and the shear behavior along the close-packed plane. The two main mechanisms will be discussed in detail in later discussion.

Figure 5b is the atomic configuration when neck finally fractures at a tip–substrate distance of 3.5 nm. A large amount of Cu atoms are transferred to nickel tip. This is due to the fact that fracture occurs in the middle of the neck, not at the interface of Ni tip and Cu substrate. Two

holes and a cluster are both observed after neck fracture. It is worth noting that adhesive force leads not only to the damage of the surface of Cu substrate but also to permanent plastic deformation deep in Cu substrate. This kind of plastic deformation is not often observed in MD models.

Discussion

Deformation Twinning

Twinning faults are observed in Cu substrate both during the indentation and retraction processes. Based on the recently proposed the GPF curve [36], we discuss the formation of twinning faults that occur during nanocontact. For FCC metals, the GPF curve represents the energy cost of rigidly shifting two semi-infinite blocks of crystal on a {111} plane along <112> direction. Here, the same strategy as in reference [37] is employed to produce the GPF curve of Cu based on the EAM potential used in our simulation. The GPF curve of Cu is plotted in Fig. 6. Unstable stacking fault energy γ_{usf} is the energy barrier that need to be crossed over for the formation of a stacking fault along the <112> direction in a perfect FCC lattice

Fig. 5 Atomic configurations of Cu substrate during the second part of retraction process at different depth: **a** $\eta = -1.56$ nm, **b** $\eta = -3.5$ nm
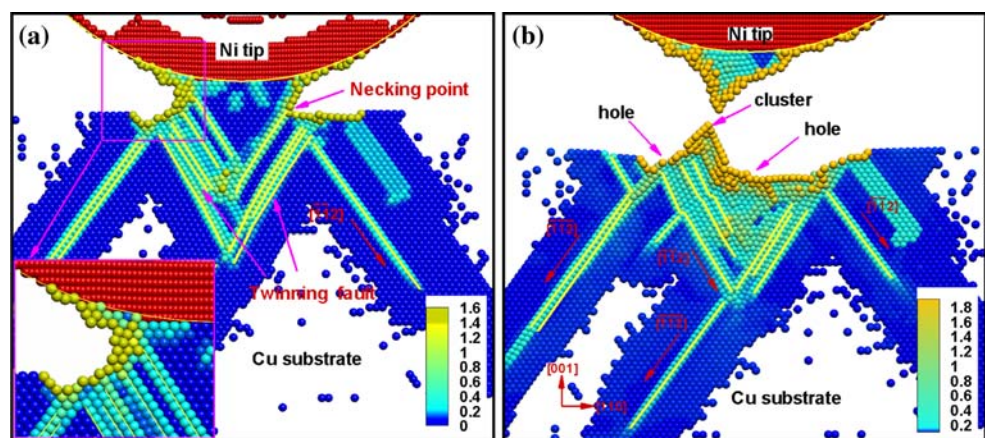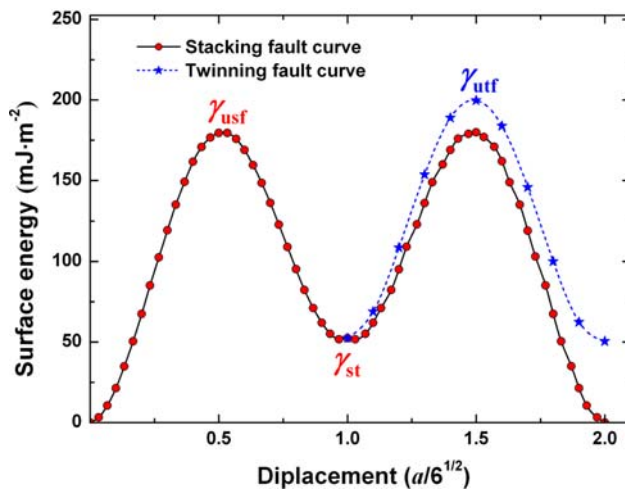
Fig. 6 Generalized planar fault energy (GPF) curves of single crystal Cu, where a is equilibrium lattice parameter

structure. Stacking fault energy γ_{sf} is the stable energy stored in a stacking fault. After a stacking fault is sustained, the adjacent plane need to overcome another energy barrier referred as unstable twining fault energy γ_{utf} for the formation of a twinning fault. Therefore, the energy necessary for the formation of a twinning fault is $\gamma_{utf}-\gamma_{sf}$. When $\gamma_{utf}-\gamma_{sf}$ is approximately equal to the energy barrier γ_{usf} for the formation of a stacking fault, stacking faults and twinning faults will both occur during nanocontact.

The calculated values of γ_{utf}, γ_{sf}, and γ_{utf} for Cu are 179.5, 52.4, and 199.8 mJ/m^2, respectively. The energy required for forming a twinning fault (namely, $\gamma_{utf}\gamma_{sf} = 147.5$ mJ/m^2) is even less than the energy required for the formation of a stacking fault ($\gamma_{utf} = 179.5$ mJ/m^2). Therefore, deformation twinning becomes an important deformation mechanism during nanocontact. In our simulation, two–three-layer twinning faults are observed beneath Ni tip at the maximum indentation depth as seen in Fig. 3d. However, compared with the twinning faults that occur

during indentation shown in Fig. 3d, more twinning faults are observed in the process of tip retraction, as shown Fig. 5a. This is not surprising if we take into account of the high stress intensity near steps of Ni tip during indentation. The close-up in Fig. 3d shows the role of high stress intensity during indentation. It can be seen that all Shockley partials emitted into Cu substrate from the steps of Ni tip where stress intensity is high. The emission of a Shockley partial from one step of Ni tip will result in stress release, while unreleased high stresses near other steps tend to trigger the emission of Shockley partials more easily. As a result, the formation of twinning fault is retarded unless sufficient energy is accumulated in the process of indentation. In the process of Ni tip retraction, stress intensity near the interface of Ni tip and Cu substrate is not very high because the steps of Ni tip are closely surrounded by Cu atoms, as shown in the inset of Fig. 5a. Without the influence of high stress intensity, the tendency of twinning formation during tip retraction is much stronger than that in the process of indentation.

Two Different Types of Fracture Mechanisms

Although sawtooth-shaped load curves are observed in nanocontact experiments during retraction [33, 35], it is difficult to directly reveal the underlying deformation mechanism through the atomic configurations. In our simulation, we find that two different types of fracture mechanisms are both responsible for load-jump during tip retraction. Based on the configurations and displacement vectors of Cu atoms during the process of neck fracture, we will discuss the two fracture mechanisms in detail.

Figure 7a illustrates the typical movement of Cu atoms near the interface corresponding to load-jump of P–Q stage in Fig. 2 during initial stage of neck elongation and fracture. Red circles and arrows represent the position and displacement vectors of atoms before load-jump, respectively. The solid spheres are the atoms after load-jump.

Fig. 7 Two different types of fracture mechanisms during the neck fracture
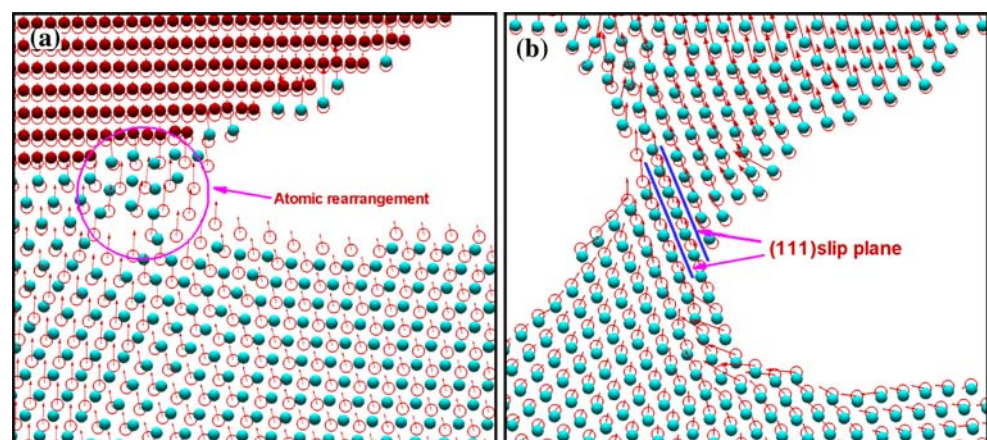
It can be seen that Cu atoms will tend to rearrange near the stepped surface of Ni tip and fill in the vacancy sites. This kind of atomic rearrangement can also be confirmed by displacement vectors. Instead of paralleling to any slip direction, most displacement vectors near the interface are perpendicular to the tip. Further retraction of Ni tip finally leads to the breakage of metallic bond and load-jump in the load–depth curve. It is worth noting that although slips of atoms along $(\bar{1}\bar{1}1)$ and (111) planes still occur in the substrate at this stage, they only lead to slight load-jumps, which are similar to load-jumps during the process of indentation as shown in Fig. 2. Therefore, atomic rearrangement is mainly responsible for the sawtooth-shaped load-jump at the initial neck-break stage.

After the rearrangement of Cu atoms on the two sides of Ni tip, the thinnest point of Cu neck happens in the middle of Cu neck, not at the interface as shown in Fig. 5a. From the stage of necking point formation to the breakage of neck, sawtooth-shaped load is mainly attributed to the shear processes on (111) plane. Displacement vectors of Cu atoms along (111) plane in Fig. 7b reveal the process of shear behavior near the necking point (corresponding to T–U stage). When the accumulated energy at the necking point reaches to critical value, the homogeneous shear suddenly occurs along (111) slip plane. Shear process is accompanied by the sudden breakage of atomic bonds on the two sides of necking point (corresponding to load-jump in the load–depth curve) and the decrease of cross-sectional area. Shear slip processes in the necking point also evidently elongate the neck till the neck fracture completely.

Analysis of Adhesive Fracture

The critical adhesive force and the critical contact radius for neck fracture occurred is one of the most important topics in adhesive contact researches. In order to further investigate the maximum adhesive force and its corresponding contact radius, a comparison between theoretical models and our results is made. One of the most important adhesive contact models is the one developed by Johnson et al. [38] (JKR model) to describe adhesive contact between a linearly elastic sphere and a flat plane. Based on the three-dimensional JKR model developed by Johnson, Chen and Wang [39] derives two-dimensional JKR adhesive contact model

$$F = -\frac{\pi E^* a^2}{4R} + \sqrt{2\pi E^* a \omega} \tag{2}$$

where F, E^*, R, a and ω are the applied load, the reduced Young's modulus, the radius of cylinder, the contact half-width and the work of adhesion, respectively. The reduced Young's modulus E^* is defined as

$$\frac{1}{E^*} = \frac{(1 - v_1^2)}{E_1} + \frac{(1 - v_2^2)}{E_2} \tag{3}$$

where E_1, v_1 and E_2, v_1 are the Young's modulus and Poisson ratio of Ni tip and Cu substrate, respectively. The work of adhesion can be expressed

$$\omega = \gamma_1 + \gamma_2 - \gamma_{12} \tag{4}$$

where γ_1, γ_2 are surface energy of two contacting surfaces, and γ_{12} is the interfacial energy. According to two-dimensional JKR model [namely, Eq. (2)], the critical load F_c and critical contact radius a_c for neck fracture occurred are

$$a_c = R^{\frac{2}{3}} \left(\frac{2\omega}{\pi E^*} \right)^{\frac{1}{3}} \tag{5}$$

$$F_c = -\frac{\pi E^* a_c^2}{4R} + \sqrt{2\pi E^* a_c \omega} \tag{6}$$

.

To take into account the effects of surface morphology and crystal orientation, the work of adhesion in our model is estimated by calculating the difference of potential energies between the starting configuration and the equilibrium configuration when the external load is zero in the process of indentation [17]. In this way, we estimated that the work of adhesion ω between Ni tip and Cu substrate is 2.23 J/m^2. By taking the radius of cylinder $R = 10$ nm and the reduced Young's modulus $E^* = 97.7$ GPa into Eqs. (5) and (6), we can get the theoretical critical load F_c and critical contact radius a_c, which are 29.5 N/m and 1.1 nm, respectively.

Comparing the earlier JKR theoretical results with our numerical results in which the critical load F and critical contact radius a are 50.6 N/m and 2.3 nm, respectively, we find that there are deviations between our numerical results and the JKR results, but it is still acceptable. In fact, due to the discrete nature of atomic-scale model, Ni tip in our simulation is not an ideal cylinder tip with a tip radius of 10 nm. The true radius of Ni tip should be larger 10 nm. Also, severe plastic deformation and material transfer which are not taken into account in elastic adhesive contact JKR model occur in our simulation. These two important factors mentioned earlier could possibly lead to deviation from theoretical results. Our later research will thoroughly examine the influence of these factors.

Conclusions

Multiscale simulation of nanocontact including the process of indentation and retraction are carried out using the quasicontinuum method. A large tip with a radius of

10 nm is chosen to mimic experimental tip in our simulation. Our research shows that plastic deformation is observed in an area as large as 20 nm wide and 10 nm thick, both in the process of indentation and retraction. The largest stacking fault extends into Cu substrate as deep as 14 nm during tip indentation. Plastic deformation deep in the Cu substrate does not disappear completely after the neck facture.

Twinning faults are also observed both in the process of indentation and retraction. The GPF curve of Cu reveals that the energy barrier $\gamma_{utf}-\gamma_{sf}$ required for the formation of deformation twinning is smaller than the energy barrier γ_{usf} required for the formation of stacking fault. However, less deformation twinning faults occur in the process of indentation than that in the process of retraction. This is a result of the high stress intensity caused by surface morphology of Ni tip. Step morphology of Ni tip retards the process of accumulating sufficient energy for emission of Shockley partials in the plane adjacent to a pre-existing stacking fault.

In agreement with experimental results, sawtooth-shaped load characterizes the process of tip retraction. Two different fracture mechanisms are responsible for load-jump at different stages of fracture. Initial stage of fracture mainly occurs at the interface between Ni tip and Cu substrate. At this stage, fracture occurs by atomic rearrangement: some Cu atoms are attracted to fill in the vacancy sites of stepped surface of Ni tip while other Cu atoms fall back to the substrate. As neck elongate, fracture occurs in the middle of Cu neck. Homogeneous shear along one (111) plane over another is the dominant fracture mechanism.

Comparing the critical adhesive force and the critical contact radius for Cu neck fracture in our simulation with JKR model, we find that there is deviation existing between theoretical values and numerical results. Several factors, such as severe plastic deformation, material transfer and the geometrical shape of Ni tip, may lead to this deviation.

References

1. B. Bhushan, J.N. Israelachvili, U. Landman, Nature **374**, 607 (1995). doi:10.1038/374607a0
2. H. Spikes, Tribol. Int. **34**, 789 (2001). doi:10.1016/S0301-679X(01)00079-2
3. B. Bhushan, Wear **259**, 1507 (2005). doi:10.1016/j.wear.2005.01.010
4. R. Maboudian, MRS Bull. **23**, 47 (1998)
5. H. Liu, B. Bhushan, J. Vac. Sci. Technol. A **21**, 1528 (2003). doi:10.1116/1.1560711
6. R. Maboudian, C. Carraro, J. Adhes. Sci. Technol. **17**, 583 (2003). doi:10.1163/15685610360554429
7. A. Fian, M. Leisch, Ultramicroscopy **95**, 189 (2003). doi:10.1016/S0304-3991(02)00316-9
8. A. Stalder, U. Dürig, Appl. Phys. Lett. **68**, 637 (1996). doi:10.1063/1.116493
9. N. Agraït, G. Rubio, S. Vieira, Phys. Rev. Lett. **74**, 3995 (1995). doi:10.1103/PhysRevLett.74.3995
10. T.B. Wei, Q. Hu, R.F. Duan, J.X. Wang, Y.P. Zeng, J.M. Li, Y. Yang, Y.L. Liu, Nanoscale Res. Lett. **4**, 753 (2009). doi:10.1007/s11671-009-9310-1
11. P.E. Marszalek, W.J. Greenleaf, H. Li, A.F. Oberhauser, J.M. Fernandez, Proc. Natl. Acad. Sci. USA **97**, 6282 (2000)
12. U. Landman, W.D. Luedtke, N.A. Burnham, R.J. Colton, Science **248**, 454 (1990). doi:10.1126/science.248.4954.454
13. U. Landman, W.D. Luedtke, J. Vac. Sci. Techno. B **9**, 414 (1991). doi:10.1116/1.585583
14. J. Song, D.J. Srolovitz, J. Appl. Phys. **104**, 124312 (2008). doi:10.1063/1.3043582
15. J. Song, D.J. Srolovitz, Acta Mater. **54**, 5305 (2006). doi:10.1016/j.actamat.2006.07.011
16. S.Y. Jiang, M.Q. Jiang, L.H. Dai, Y.G. Yao, Nanoscale Res. Lett. **3**, 524 (2008). doi:10.1007/s11671-008-9192-7
17. J.H.A. Hagelaar, E. Bitzek, C.F.J. Flipse, P. Gumbsch, Phys. Rev. B **73**, 045425 (2006). doi:10.1103/PhysRevB.73.045425
18. M.G. Boyle, F. Lei, P. Dawson, Ultramicroscopy **108**, 558 (2008). doi:10.1016/j.ultramic.2007.08.012
19. D. Gingery, P. Bühlmann, Rev. Sci. Instrum. **78**, 113703 (2007). doi:10.1063/1.2804132
20. C.T. Wang, S.R. Jian, J.S.C. Jang, Y.S. Lai, P.F. Yang, Appl. Surf. Sci. **255**, 3240 (2008). doi:10.1016/j.apsusc.2008.09.034
21. W.A. Curtin, R.E. Miller, Modelling. Simul. Mater. Sci. Eng. **11**, R33 (2003). doi:10.1088/0965-0393/11/3/201
22. S.P. Xiao, T. Belytschko, Comput. Methods Appl. Mech. Eng. **193**, 1645 (2004). doi:10.1016/j.cma.2003.12.053
23. R.E. Miller, E.B. Tadmor, Modelling Simul. Mater. Sci. Eng. **17**, 053001 (2009). doi:10.1088/0965-0393/17/5/053001
24. E.B. Tadmor, M. Ortiz, R. Phillips, Philos. Mag. A **73**, 1529 (1996). doi:10.1080/01418619608243000
25. V.B. Shenoy, R. Miller, E.B. Tadmor, D. Rodney, R. Phillips, M. Ortiz, J. Mech. Phys. Solids **47**, 611 (1999). doi:10.1016/S0022-5096(98)00051-9
26. J.W. Li, Y.S. Ni, H.S. Wang, J.F. Mei, Nanoscale Res. Lett. (2009), Online first, doi:10.1007/s11671-009-9500-x
27. M.S. Daw, M.I. Baskes, Phys. Rev. B **29**, 6443 (1984). doi:10.1103/PhysRevB.29.6443
28. R.L. Hayes, M. Fago, M. Ortiz, E.A. Carter, Multiscale Model. Simul. **4**, 359 (2005)
29. M.L. Trouwborst, E.H. Huisman, F.L. Bakker, S.J. van der Molen, B.J. van Wees, Phys. Rev. Lett. **100**, 175502 (2008). doi:10.1103/PhysRevLett.100.175502
30. J. Jin, S.A. Shevlin, Z.X. Guo, Acta Mater. **56**, 4358 (2008). doi:10.1016/j.actamat.2008.04.064
31. J. Li, K.J. Van Vliet, T. Zhu, S. Yip, S. Suresh, Nature **418**, 307 (2002). doi:10.1038/nature00865
32. R.E. Miller, D. Rodney, J. Mech. Phys. Solids **56**, 1203 (2007). doi:10.1016/j.jmps.2007.10.005
33. G. Rubio, N. Agraït, S. Vieira, Phys. Rev. Lett. **76**, 2302 (1996). doi:10.1103/PhysRevLett.76.2302
34. R. Erlandsson, V. Yakimov, Phys. Rev. B **62**, 13680 (2000). doi:10.1103/PhysRevLett.80.4685

35. G. Cross, A. Schirmeisen, A. Stalder, P. Grütter, Phys. Rev. Lett. **80**, 4685 (1998). doi:10.1103/PhysRevLett.76.2302
36. H. Van Swygenhoven, P.M. Derlet, A.G. Frøseth, Nature Mater. **3**, 399 (2004). doi:10.1038/nmat1136
37. J.A. Zimmerman, H. Gao, F.F. Abraham, Modelling. Simul. Mater. Sci. Eng. **8**, 103 (2000). doi:10.1088/0965-0393/8/2/302
38. K.L. Johnson, K. Kendall, A.D. Roberts, Proc. R. Soc. London. Ser. A **324**, 301 (1971)
39. S. Chen, T. Wang, J. Colloid Interface Sci. **302**, 363 (2006). doi:10.1016/j.jcis.2006.06.014